

Hydrophobic Periphery Tails of Polyphenylenepyridyl Dendrons Control Nanoparticle Formation and Catalytic Properties

Nina V. Kuchkina,[†] David Gene Morgan,[‡] Athanasia Kostopoulou,^{||} Alexandros Lappas,^{||} Konstantinos Brintakis,^{||,⊥} Bethany S. Boris,[‡] Ekaterina Yu. Yuzik-Klimova,[†] Barry D. Stein,[§] Dmitri I. Svergun,[#] Alessandro Spilotros,[#] Mikhail G. Sulman,[▽] Linda Zh. Nikoshvili,[▽] Esther M. Sulman,[▽] Zinaida B. Shifrina,^{*,†} and Lyudmila M. Bronstein^{*,‡,○}

[†]A.N. Nesmeyanov Institute of Organoelement Compounds, Russian Academy of Sciences, 28 Vavilov St., Moscow, 119991 Russia

[‡]Department of Chemistry and [§]Department of Biology, Indiana University, Bloomington, Indiana 47405, United States

^{||}Institute of Electronic Structure and Laser, Foundation for Research and Technology – Hellas, 71110 Heraklion, Crete, Greece

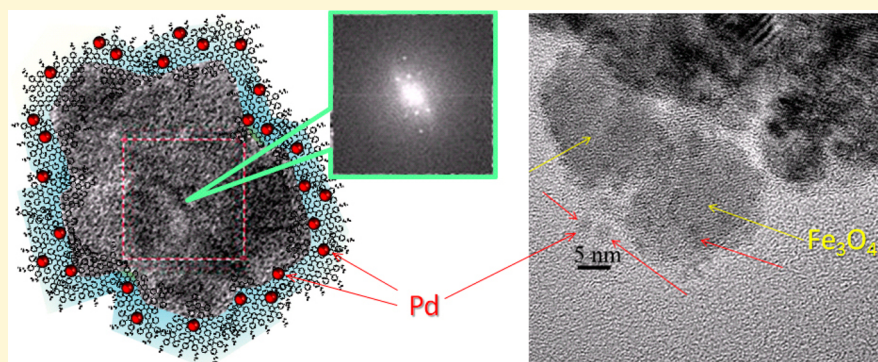
[⊥]Department of Physics, Aristotle University of Thessaloniki, 54124 Thessaloniki, Greece

[#]EMBL, Hamburg Outstation, Notkestraße 85, D-22603 Hamburg, Germany

[▽]Department of Biotechnology and Chemistry, Tver State Technical University, 22 A. Nikitina St., 170026, Tver, Russia

[○]Department of Physics, Faculty of Science, King Abdulaziz University, Jeddah, Saudi Arabia

Supporting Information

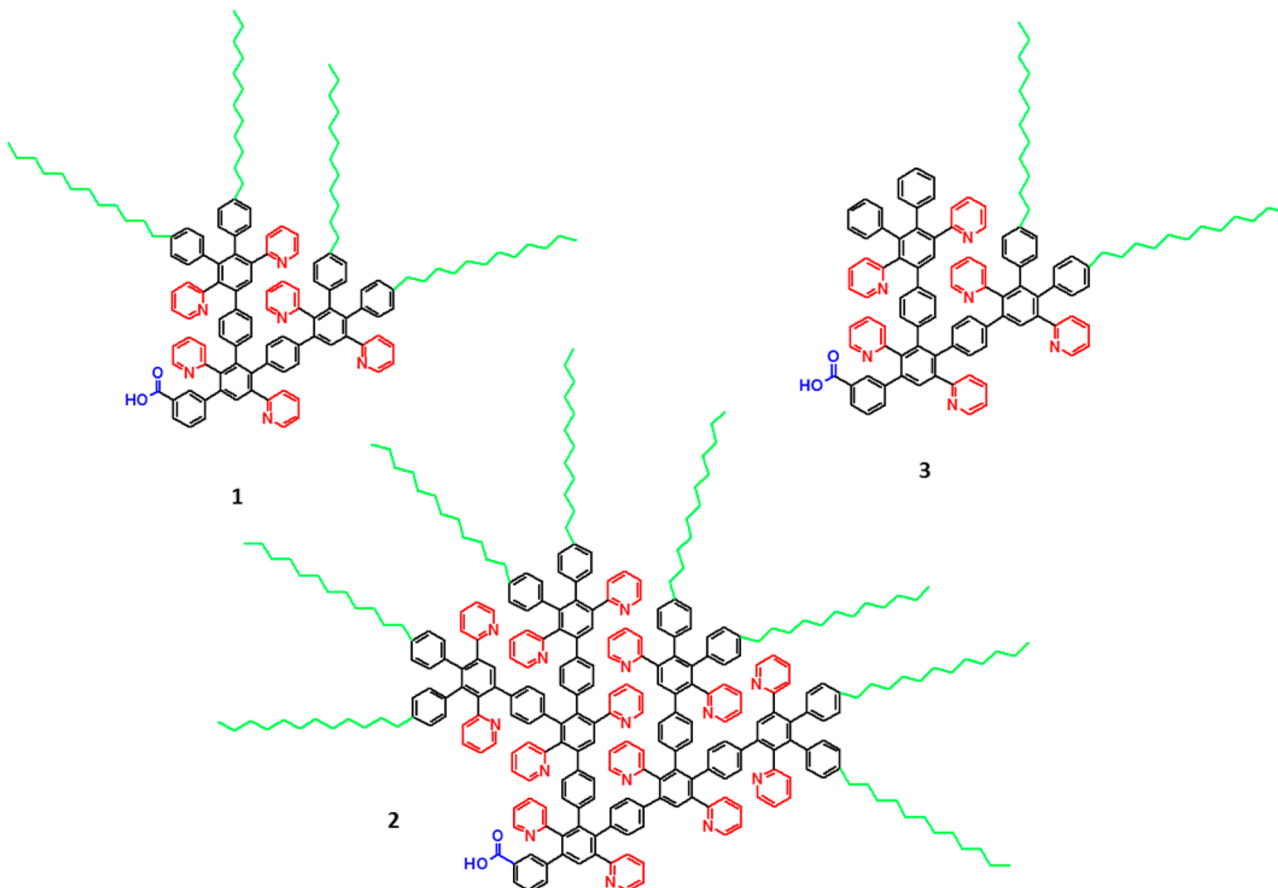


ABSTRACT: Here we report control of iron oxide and palladium nanoparticle (NP) formation via stabilization with polyphenylenepyridyl dendrons of the second and third generations with dodecyl periphery. These nanomaterials are developed as magnetically recoverable catalysts. To accurately assess the influence of the dodecyl exterior for the same dendron generation, we also designed a second generation dendron with partial dodecyl periphery. For all dendrons studied, the multicore iron oxide mesocrystals were formed, the sizes and morphology of which were controlled by the dendron generation. Analysis of the static and dynamic magnetic properties, in combination with transmission electron microscopy observations, demonstrate that magnetism is sensitive on the structure-directing capabilities of the type of the dendron which was employed for the mesocrystal stabilization. Close proximity of single cores in such multicore mesocrystals promotes the coupling of the neighboring magnetic moments, thus boosting their magnetization and allowing easy crossover between superparamagnetic and ferrimagnetic behaviors at room temperature. The particularly dramatic role of the dendron structure was also witnessed via the Pd NP formation, which was found to depend on both the dendron generation and its dodecyl periphery. In the case of the catalyst based on the second generation dendron with full dodecyl periphery, no Pd NPs were observed by TEM indicating that these species are of a subnanometer size and are not visible on or near the iron oxide NPs. For the catalyst based on the second generation dendron with partial dodecyl periphery, hydrogen reduction leads to much larger Pd NPs (2.7 nm) due to an unimpeded exchange of Pd species between dendrons and nondense dendron coating with asymmetrical dendrons. The third generation dendron with full dodecyl periphery allows nearly monodisperse 1.2 nm Pd NPs in the shells of iron oxide mesocrystals and the best catalytic properties in selective hydrogenation of dimethyl-ethynylcarbinol. This study suggests a robust approach to control NP formation in magnetically recoverable catalysts for a wide variety of catalytic reactions using dendrons combining rigidity and flexibility in one molecule.

Received: June 27, 2014

Revised: September 5, 2014

Published: September 8, 2014

Scheme 1. Formulas of Dendrons 1 (a), 2 (b), and 3 (c)^a

^aPyridine rings are shown in red, phenylene rings are in black, and a carboxyl focal group is shown in blue. Dodecyl chains are in green.

■ INTRODUCTION

Although numerous active and selective homogeneous catalysts are described in literature, less than 20% of such processes are used in industry while heterogeneous catalysis is clearly prevailing.¹ This should be ascribed to the difficulty of the separation of homogeneous catalysts from reaction solutions. The separation can be performed, as is discussed in a recent review,² but it is time and energy consuming. In recent years a combination of catalytic species and magnetic NPs has been suggested which allows robust and inexpensive magnetic separation of catalysts.^{3–10} Earlier we reported magnetically controllable catalysts where magnetic iron oxide nanoparticles (NPs) were synthesized using polyphenylenepyridyl dendrons and dendrimers with mixed pyridyl–phenylene or purely pyridyl periphery as capping molecules.^{11,12} Dendrimers are complex monodisperse macromolecules with a regular and highly branched three-dimensional architecture and well-defined chemical structure.^{2,13,14} Dendrons are essentially wedges or slices of a dendrimer and due to coordination groups in a focal point they are especially suited as ligands during NP formation.¹⁵ The benefit of synthesizing iron oxide NPs directly in the presence of functional dendrons vs ligand exchange is that the dendron adsorbs on the NP surface upon formation and makes NPs evenly functionalized. In other words, the NP is already formed well dispersed and no further functionalization is required. Although in our preceding work^{11,12} we were able to influence the Pd NP size and the catalytic properties varying the structure of these dendrons/dendrimers and the reaction conditions, the ion exchange between

the dendrons/dendrimers when iron oxide or Pd NPs were formed did not allow us to single out key parameters which would be crucial for the control of the catalyst formation properties.

For conventional dendrons and dendrimers, it was reported that inert tails in the periphery prevent interdendrimer interactions via complexation with metal ions but also add steric protection to single dendrimers. This results in prevention of metal ion exchange between dendrimers and formation of dendrimer encapsulated small monodisperse NPs.^{16–18} It is demonstrated that NPs designed for catalytic applications should be sufficiently small to have a large surface area with many active centers, but at the same time, not too small because of unfavorable curvatures for adsorption of reacting molecules^{19–22} or a different character of NPs (semiconductor vs metallic) which changes catalytic center properties.²³ Thus, an optimal catalytic NP size is required. However, in complex composite materials control over catalytic NP formation is rarely achieved.

Here we report formation of multicore iron oxide mesocrystals stabilized by polyphenylenepyridyl dendrons of the second and third generations with dodecyl chains in the periphery (Scheme 1). The iron oxide mesocrystals display ferrimagnetic behavior at room temperature and possess shell functionality due to pyridine groups. We demonstrate that these dendrons control both iron oxide NP morphology and the sizes of Pd NPs. Moreover, this control is carried out via a rational design of the dendron structure, i.e., both periphery and generation. To probe the influence of the number of hydrophobic chains in the periphery, we designed, for the first time, a second generation dendron with partial dodecyl

periphery (Scheme 1). It is established here that the Pd NP size dramatically influences the catalytic properties tested in selective hydrogenation of dimethylethylnylcarbinol (DMEC) to dimethylvinylcarbinol (DMVC).

EXPERIMENTAL SECTION

Materials. Iron(III) acetylacetone (99+%) was purchased from Acros Organics and was used as received. Palladium(II) acetate was purchased from Strem Chemicals and also used as received. Superhydride solution (1.0 M lithium triethylborohydride in THF), benzyl ether (98%), and the Lindlar catalyst (Pd/CaCO₃ poisoned by lead) were purchased from Sigma-Aldrich and used without purification. Acetone (99.5%) and chloroform (99.8%) were purchased from MACRON Chemicals and used as received.

Synthetic Procedures. *Synthesis of Dendrons.* Syntheses of dendrons 1 and 2 were described in our preceding paper.¹¹ Dendron 3 was synthesized according to the procedure described in the Supporting Information (Scheme S1).

Synthesis of Iron Oxide Nanoparticles. In a typical procedure, the three-neck round-bottom flask (with elongated necks) equipped with a magnetic stir bar, a reflux condenser, and two septa, one of which contained an inserted temperature probe protected with a glass shield and the other had a long inserted needle, was loaded with 0.353 g (1 mmol) of Fe(acac)₃, 0.427 g (0.22 mmol) of dendron 1, and 7 mL of benzyl ether. The flask was placed in a Glas-Col heating mantle attached to a digital temperature controller which in turn was placed on a magnetic stirrer. The flask was degassed by argon bubbling for 30 min under stirring. Then the temperature was raised to 60 °C at 10°/min and kept under stirring at this temperature for 30 min to allow solubilization. Then the temperature was increased with a heating rate 10°/min, and the flask was allowed to reflux for 1 h at 283–285 °C. The flask was then removed from the heating mantle and allowed to cool to room temperature. To isolate NPs, a part of the reaction solution was precipitated by ethanol and washed several times with ethanol and acetone until colorless and transparent supernatant was obtained. The latter was removed, while the precipitate was dispersed in chloroform upon sonication for 20 min. No aggregates were formed with dendrons 1–3 unlike other dendrons or dendrimers described elsewhere.¹² The yield of iron oxide NPs was in the range 87–90%. The rest of the reaction solution was stored in a refrigerator and was stable for many months. This sample is denoted NP1-1. “NP” stands for iron oxide NPs; the first number indicates the specific dendron according to Scheme 1, and the second number indicates the synthesis number according to Table 1.

Table 1. Characteristics of Iron Oxide NP Stabilized by Dendrons with Dodecyl Periphery

NP notation	dendron amount ^a (g/mmol)	NP size (nm)	standard deviation (%)
NP1-1	0.427/0.22	24.5	20.8
NP1-2	0.214/0.11	22.6	16.8
NP1-3	0.107/0.055	18.8	20.7
NP2-1	0.912/0.22	31.6	13.3
NP3-1	0.274/0.22	21.6	21.3

^aLoading of other reagents: 0.353 g (1 mmol) of Fe(acac)₃, 7 mL of benzyl ether.

This table lists the reaction conditions and the sizes of the iron oxide NPs formed with all three dendrons.

Methods. Electron-transparent NP specimens for transmission electron microscopy (TEM) were prepared by placing a drop of dilute solution onto a carbon-coated Cu grid. Images were acquired at an accelerating voltage of 80 kV on a JEOL JEM1010 transmission electron microscope. Images were analyzed with the National Institute of Health developed image-processing package ImageJ to estimate NP diameters. Between 150 and 300 NPs were used for this analysis. High resolution TEM (HRTEM), tomography, and energy dispersive X-ray spectra

(EDS) were acquired at accelerating voltage 300 kV on a JEOL 3200FS transmission electron microscope equipped with an Oxford Instruments INCA EDS system. The same TEM grids were used for all analyses.

X-ray fluorescence measurements to determine the Pd content were performed with a Zeiss Jena VRA-30 spectrometer (Mo anode, LiF crystal analyzer and SZ detector). Analyses were based on the Co K α line and a series of standards prepared by mixing 1 g of polystyrene with 10–20 mg of standard compounds. The time of data acquisition was constant at 10 s.

X-ray diffraction (XRD) patterns were collected on an Empyrean from PANalytical. X-rays were generated from a copper target with a scattering wavelength of 1.54 Å. The step-size of the experiment was 0.02.

The magnetic properties of the samples were studied by a Superconducting Quantum Interference Device (SQUID) magnetometer (Quantum Design MPMS XLS). The measurements have been performed in dried nanoparticles on cotton in a gelatin capsule. The isothermal hysteresis loops, $M(H)$, were measured at fields $-1 \leq H \leq +1$ T. The dc magnetic susceptibility as a function of temperature, $\chi(T)$, was attained down to 5 K under zero-field cooled (ZFC) and field-cooled (FC) protocols, at $H = 50$ Oe. The frequency dispersion of the ac susceptibility ($f = 0.099, 0.999, 9.999, 100.024$, and 997.34 Hz; ac field 1 Oe) was also recorded as a function of temperature. Suitable phenomenological models (eqs S1–S3, Supporting Information) were tested against the temperature evolution of the relaxation time, $\tau = (2\pi f)^{-1}$. The position of the maximum in the dissipative part of the ac susceptibility, $\chi''(T)$, was determined as the temperature at which the first derivative of χ'' becomes zero.

The X-ray scattering data have been collected at the P12 beamline of the European Molecular Biology Laboratory (EMBL) on the storage ring Petra III of the Deutsches Elektronen Synchrotron (DESY, Hamburg). Using a Pilatus2M detector (Dectris, Switzerland), the scattering was recorded in the range of the momentum transfer $0.07 < s < 4.3$ nm⁻¹, where $s = 4\pi \sin \theta/\lambda$, 2θ is the scattering angle, and $\lambda = 0.1$ nm is the X-ray wavelength.

Dendrons 1 and 2 have been dissolved in tetrahydrofuran (THF) at three different concentrations (10, 5, and 2.5 mg/mL). The solutions were then measured with exposure time of 1 s in a vacuum capillary to diminish the parasitic scattering. The scattering profiles were corrected for the background scattering from the THF solvent and processed using an automated pipeline.²⁴ The concentration series has been used to check for interparticle interactions and to extract the structural parameters corresponding to infinite dilution.²⁴ The distance distribution functions $P(r)$ were calculated using an indirect Fourier transform program GNOM.²⁵

The low-resolution shapes of the dendron ensembles were reconstructed ab initio from the scattering patterns by DAMMIF.²⁶ This program represents the object as an assembly of beads inside a spherical search volume. Starting from a random assembly, DAMMIF employs simulated annealing to build compact scattering equivalent models fitting the experimental data $I_{\text{exp}}(s)$ to minimize discrepancy:

$$\chi^2 = \frac{1}{N-1} \sum_j \left[\frac{I_{\text{exp}}(s_j) - c I_{\text{calc}}(s_j)}{\sigma(s_j)} \right]^2 \quad (1)$$

where N is the number of experimental points, c a scaling factor, and $I_{\text{calc}}(s_j)$ and $\sigma(s_j)$ are the calculated intensity from the model and the experimental error at the momentum transfer s_j , respectively.

The content of aggregates in the two samples was estimated by the analysis of the forward scattering intensity I_0 and the radii of gyration of the monomers (self-assembled compact particles) R_{gmono} and aggregates R_{gagg} . For the monomer scattering, $I_{0\text{mono}} \sim N_{\text{mono}}(V_{\text{mono}})^2$ where N is the number of monomers and V their volume. The forward scattering from the aggregates can be estimated as $I_{0\text{agg}} = I_{0\text{whole}} - I_{0\text{mono}}$ where $I_{0\text{whole}}$ is the forward scattering of the entire system. Taking into account that the number of monomers in an aggregate k is approximately $k \sim (V_{\text{Agg}}/V_{\text{mono}})$, the volume fraction of compact particles is calculated as $\nu_{\text{mono}} = k(I_{0\text{mono}}/I_{0\text{agg}})/(1 + k(I_{0\text{mono}}/I_{0\text{agg}}))$.

Catalytic Studies. Catalytic testing was carried out in a 60 mL isothermal glass batch reactor installed in a shaker and connected to a

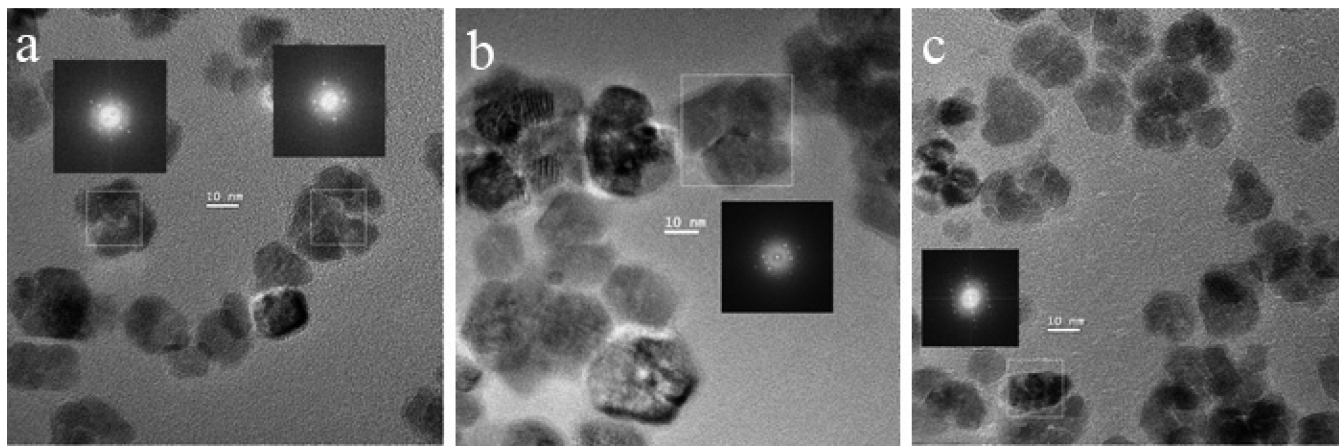


Figure 1. HRTEM images of iron oxide NPs formed in the presence of dendrons 1 (a), 2 (b), and 3 (c) as capping molecules. Insets show FFT patterns of the HRTEM images.

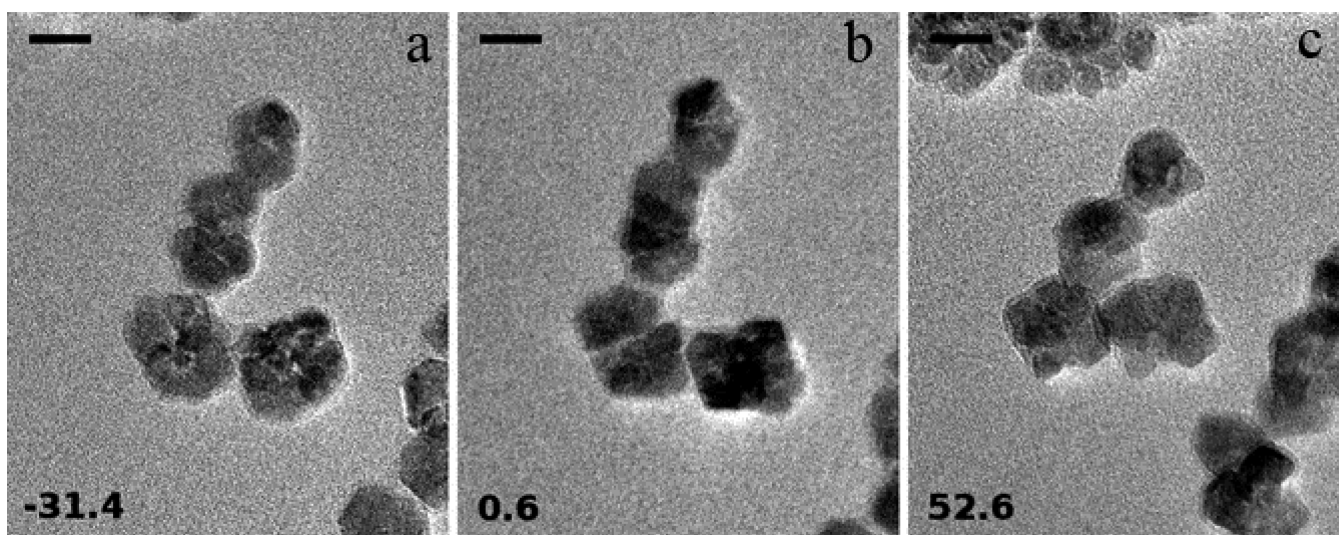


Figure 2. TEM tomography projections for NP2-1 at -31° (a), 0.6° (b), and -52.6° (c). Scale bar is 20 nm.

gasometrical buret (for a hydrogen consumption control). The total volume of the liquid phase was 30 mL. Reaction conditions were as follows: ambient hydrogen pressure, stirring rate of 850 shakings per minute, temperature 90 °C. Toluene was used as a solvent.

Probes were periodically taken and analyzed via GC-MS (Shimadzu GCMS-QP2010S) equipped with a capillary column HP-1MS (30 m × 0.25 mm i.d., 0.25 μm film thickness). Helium was used as a carrier gas at flow rate 1 mL/min. Analysis conditions: oven temperature 60 °C (isothermal), injector and interface temperature 280 °C, ion source temperature 260 °C, range from 10 up to 200 *m/z*.

Selectivity to DMVC was defined as $S_{\text{DMVC}} = Y_{\text{DMVC}} \times X^{-1} \times 100\%$, where X is the DMEC conversion and Y_{DMVC} is the DMVC yield. Activity was calculated as $\text{TOF} = C_{\text{DMEC}} \times C_{\text{Pd}}^{-1} \times \tau^{-1}$, where C_{DMEC} and C_{Pd} are the molar amounts of DMEC and Pd and τ is the reaction time. It is noteworthy that the molar ratio of DMEC to Pd was about 31000 mol/mol for all the catalytic systems.

RESULTS AND DISCUSSION

We studied the influence of hydrophobic periphery of the second and third generation dendrons on the possibility to control the iron oxide and Pd NP formation in the dendron environment. The former NPs are the support for magnetically recoverable catalysts, while the latter ones provide catalytic centers. In addition to exploring full dodecyl periphery in **1** and **2** and assessing the influence of the dendron generation, we also designed a new

second generation dendron **3** with partial dodecyl periphery to evaluate the influence of the amount of hydrophobic tails for the same dendron generation.

Influence of Dodecyl Periphery on the Iron Oxide Nanoparticle Formation. HRTEM and TEM images of iron oxide NPs prepared in the presence of dendrons **1**, **2**, and **3** as capping molecules are presented in Figure 1 and Figure S1 (Supporting Information). These iron oxide NPs display mainly multicore, flower-like morphologies.²⁷ Only a few single core spherical NPs were observed in NP1-1 and NP3-1, while in NP2-1 they are nearly absent. This is in contrast with the majority of iron oxide NP samples formed in the presence of phenylene-pyridyl dendrons and dendrimers with mixed phenylene-pyridyl periphery,¹² where the mixture of single and multicore NPs was observed. Fast Fourier Transform (FFT) patterns of multicore NPs shown in the insets of Figure 1 demonstrate single crystalline orientation. The XRD patterns reveal that the iron oxide NPs are magnetite (Figure S2, Supporting Information). The tomography images for NP2-1 presented in Figure 2 and video S1 (Supporting Information) show that multicore NPs are 3D structures and there are spaces between single cores, thus revealing that these NPs are mesocrystals.^{28–30} The close look at Figure 2a shows two characteristic distances for the NP2-1

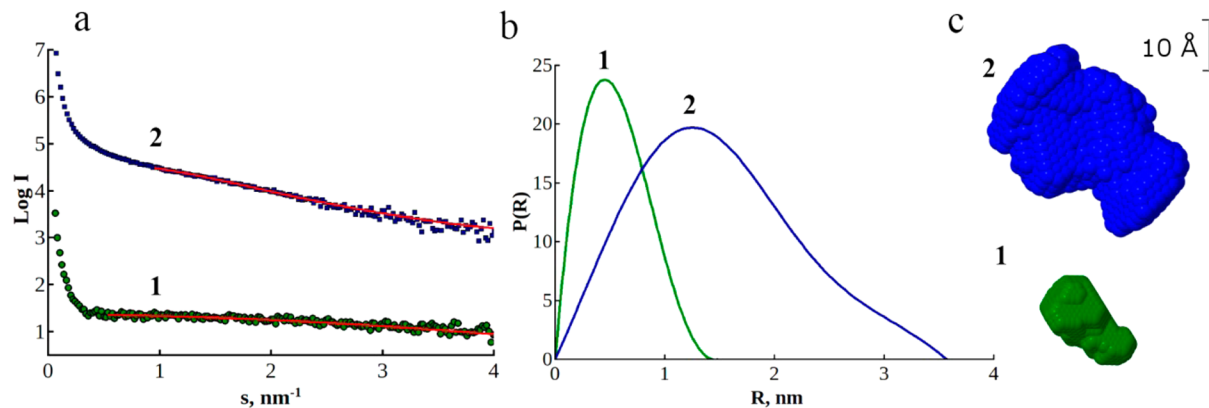


Figure 3. (a) Experimental data (one point out of every eight is displayed) and the scattering patterns computed from the ab initio model (lines) for 1 and 2. The appropriate interval was selected for the fitting in order to exclude any interparticle interactions. (b) Distance distribution functions computed by GNOM for 1 and 2. (c) Three dimensional models obtained by DAMMIN corresponding to dendrons 1 and 2.

sample: 2 nm in the center of the multicore particle and 0.8 nm along the connecting single cores. For NP1-1, only a single distance of 0.8 nm is observed (Figure S3, Supporting Information) as was described in our preceding paper.²⁷ Evidently, larger NP2-1 consists of larger single cores whose fitting in a multicore NP requires a larger distance in the center.

Thus, the presence of flexible hydrophobic tails in the rigid dendron periphery does not prevent oriented attachment of single cores (necessary condition of mesocrystal formation)²⁸ but rather facilitates it.

The data presented in Table 1 show that, for dendrons with dodecyl periphery, the iron oxide NP sizes can be somewhat influenced by varying the dendron loading (samples NP1-1, NP1-2, and NP1-3, see Figure S4, Supporting Information) and the dendron periphery (compare NP1-1 and NP3-1). On the other hand, the NP sizes are strongly affected when the dendron generation is varied (compare NP1-1 and NP2-1). The TGA traces of NP1-1 and NP1-2 (Figure S5, Supporting Information) demonstrate that iron oxide NPs prepared at lower dendron loading contain less stabilizing molecules on their surface, but no other changes in thermal behavior were observed.

In all cases, the iron oxide NPs were colloidally soluble in chloroform for weeks and easily dispersible again if chloroform had evaporated. Moreover, even the much larger iron oxide NPs shown in Figure 1b are well dispersed in solution without aggregation. This is a striking difference with iron oxide NPs stabilized with dendrons having mixed phenylene–pyridyl periphery where larger multicore NPs are usually aggregated.¹² Therefore, the hydrophobic periphery here allows much better stabilization of iron oxide NPs, preventing aggregation.

The mechanism of the multicore (flower-like) iron oxide mesocrystal formation in the case of the dendrimer with mixed phenylene–pyridyl periphery as a capping molecule was discussed in ref 27, based on the TEM analysis of the specimens withdrawn from the reaction solution when the temperatures reached 250 and 270 °C and in 15 min at 285 °C (reaction temperature).

According to this mechanism, seeds (small NPs) form at 250 °C, and then at 270 °C they become oriented due to the dendrimer self-assembly and start growing into larger single cores due to fusion. Further, the single cores are oriented in a single crystallographic pattern assisted by the dendrimer but without fusion leading to multicore mesocrystals. For dendron 1, we also withdrew specimens at different temperatures; however, at 250 °C the multicore NP formation had already taken place

(Figure S6c, Supporting Information), so additional specimens were taken in the other procedure at 200 and 225 °C. The TEM images of all these specimens presented in Figure S6 (Supporting Information) show a similar mechanism, but the Fe(acac)₃ decomposition with the formation of seeds was actively happening already by 200 °C: not only seeds but also single cores can be observed at this temperature. According to ref 29, in the solid state Fe(acac)₃ decomposes at 182 °C. Thus, dendron 1 facilitates the Fe(acac)₃ decomposition compared to the dendrimer studied earlier.²⁷

SAXS Study of the Solution Behavior of Dendrons 1, 2, and 3. To assess the relationship between the solution behavior of dendrons and multicore NP formation, dendrons 1 and 2 were examined by SAXS. The experimental scattering profiles from 1 and 2 are displayed in Figure 3, and the structural parameters obtained from the data analysis are summarized in Table S1 (Supporting Information). The SAXS profiles in Figure 3 display sharp upturns at very small angles ($s < 0.5 \text{ nm}^{-1}$), which indicate that large clusters or aggregates coexist in solution with smaller particles. The low resolution structure of the individual particles can be reconstructed from the higher-angle portions of the scattering data beyond the influence of the aggregates. The appropriate intervals of the experimental curves were processed by GNOM to compute the distance distribution functions (Figure 3b) and used in the modeling procedure. The latter functions were backtransformed to extrapolate the scattering from the individual particles to zero angle, and low resolution shapes were further reconstructed ab initio by DAMMIN³¹ (Figure 3c). While dendron 1 exhibits a globular shape, dendron 2 has an elongated shape, and the typical models yield good fits to the experimental data with discrepancy $\chi = 1.0$ and 1.3, respectively (Figure 3). Dendron 1 shows a small and compact structure in solution with a maximum linear dimension of 1.4 nm. This dimension is close to an individual dendron size. Alternatively, dendron 2 forms column-like structures with a diameter of about 1.3 nm and a height of 4 nm, suggesting the dendron self-assembly. It is noteworthy that dodecyl chains do not contribute into the SAXS scattering because of their low density.

The fraction of large aggregates in the case of dendrons 1 does not exceed 2 vol %, while for dendrons 2, the fraction of aggregates is much larger (22 vol %), although the cluster size is close. The number of individual dendron particles in a cluster is given by the ratio $V_{\text{cluster}}/V_{\text{mono}}$ and varies from about 2.3×10^5 for dendron 1 to 0.3×10^5 for dendron 2.

These data demonstrate that dendron **2** has much higher propensity to self-assemble and to aggregate. According to our preceding paper,²⁷ this tendency is consistent with the formation of a higher fraction of multicore NPs and larger NPs in the case of **2**.

Spin Dynamics and Ferrimagnetism in Iron Oxide Multicore Mesocrystals.

In multicore mesocrystals, the controlled oriented attachment of single core NPs increases their proximity and promotes the coupling of the neighboring magnetic moments. This coupling boosts magnetization and ferrimagnetic behavior at room temperature and may allow an easy crossover between superparamagnetic and ferrimagnetic behavior.

To assess the magnetic behavior of these multicore mesocrystals, initially, dc magnetic measurements were carried out for NP1-1, NP2-1, and NP3-1. The temperature dependence of the dc susceptibility, $\chi(T)$, is shown in Figure 4a. It is worth noting the presence of two broad humps in ZFC curves, one at $T_{\max,h}$ (~ 300 K) and a weaker one at $T_{\max,l}$ (~ 40 K). $T_{\max,h}$ can be attributed to the blocking temperature of the superspins of the mesocrystals, and this should be affected by intramesocrystal characteristics (e.g., dipolar interactions between the single cores and intraparticle exchange interactions).³² For NP1-1 and NP3-1, the blocking temperatures are nearly the same due to the comparable NP sizes (24.5 and 21.6 nm, respectively, Table 1), while it is higher for NP2-1 whose mean size is 31.6 nm. At the same time, the blocking temperatures for all the samples are above 300 K, revealing that they are ferrimagnetic at room temperature. Similar ferrimagnetic behavior has been observed for magnetite NPs in our preceding paper²⁷ and for maghemite nanoparticle assemblies capped with poly(acrylic) acid.³² In the latter case, it was assigned to intracluster characteristics. This is also in agreement with the nonzero coercive field, H_C , derived from the isothermal magnetization curves at the same temperature presented in Figure 4b. The smaller coercive field at 5 K, where the thermal agitation is reduced, for the largest diameter sample NP2-1 (Figure 4c), is evidence for stronger dipolar interactions compared to the other samples that are stabilized with dendrons of the second generation. This is in agreement with the extended plateau in the FC $\chi(T)$ curve (Figure 4a curves with filled symbols), as it has been suggested before on the basis of experimental studies supported by Monte Carlo simulations in relevant systems of assembled NPs.³²

Furthermore, it is worth noting the presence of the weak broad hump at $T_{\max,l}$ for the samples NP2-1 and NP3-1 while this feature is absent in the case of NP1-1, the origin of which required further investigation. Therefore, the frequency dependence of the ac susceptibility has been measured down to 5 K for the sample (NP2-1) with the more prominent cusp around $T_{\max,l}$. The real $\chi'(T)$ and the imaginary $\chi''(T)$ parts of the susceptibility are shown in Figure 5. Two features in the imaginary part of the susceptibility, $\chi''(T)$, are particularly interesting; a sharper peak at $T_{\max,l} \sim 40$ K and a much broader one at $T_{\max,h} \sim 280$ K. Similar dynamic behavior has been observed in systems such as nickel ferrite,³³ NiO,³⁴ and Co₅₀Ni₅₀³⁵ NPs, where the high-temperature feature was attributed to the blocking temperature of the superspins, while the low-temperature one was attributed to the freezing of the surface spins.

In order to further understand the origin of the dynamic susceptibility anomalies, one needs to consider the temperature dependence of the characteristic relaxation times, τ , as they are evaluated from the frequency dependence of the $\chi''(T)$ maximum. This was proven to be very informative for the low-temperature magnetic regime when we assessed the dynamics

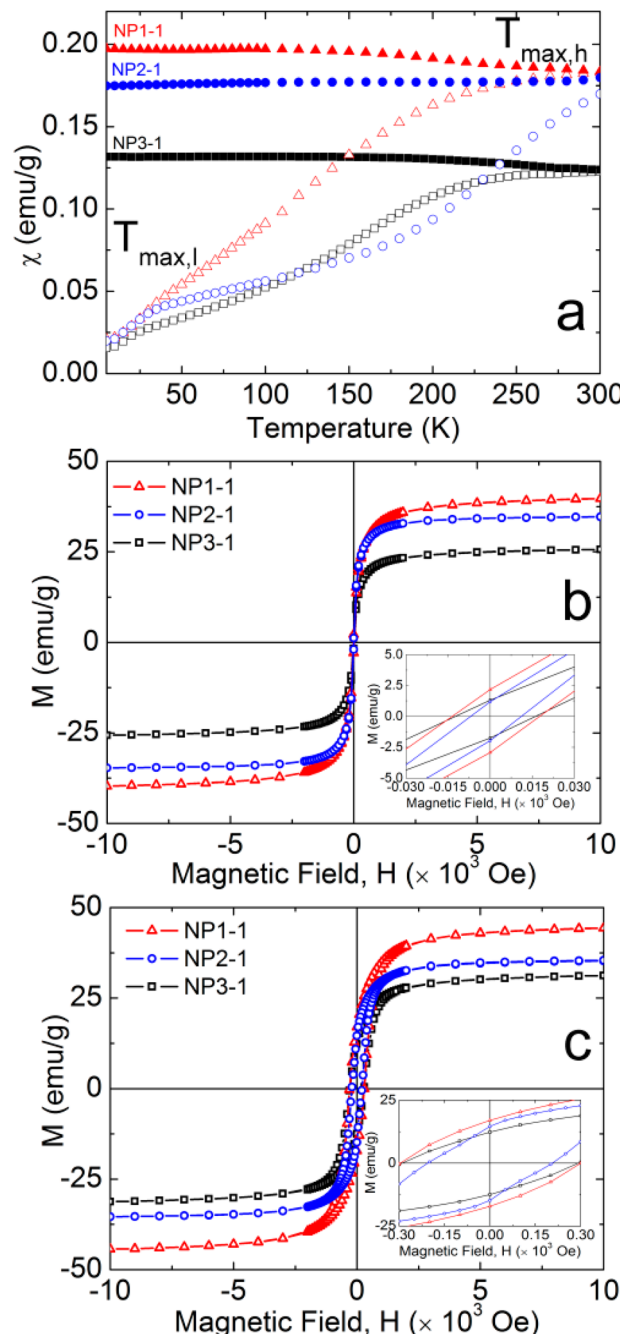


Figure 4. ZFC–FC dc susceptibility, $\chi(T)$, curves (open and filled symbols, respectively) as a function of temperature under a magnetic field of 50 Oe (a) and isothermal magnetization curves at 300 K (b) and 5 K (c) for NP1-1 (triangles), NP2-1 (circles), and NP3-1 (squares).

after successful fitting attempts with the Arrhenius,³⁶ Vogel–Fulcher,³⁷ and power-law phenomenological descriptions (Figure S7, Supporting Information and Table 2).³⁸

It appears that the frequency dependence of the $\chi''(T)$ maximum at $T_{\max,l}$ does not follow the Arrhenius law (eq S1 and Figure S7a, Supporting Information), which normally describes the temperature dependence of the characteristic relaxation time, τ , in particulate systems with very weak interparticle interactions. The fit value obtained for the activation energy, E_a/k_B (= 420 K) (Table 2), was found to be large with respect to the energy scale ($k_B T$) in this low-temperature regime. It implies that in the multicore mesocrystal the dipolar interactions among the single

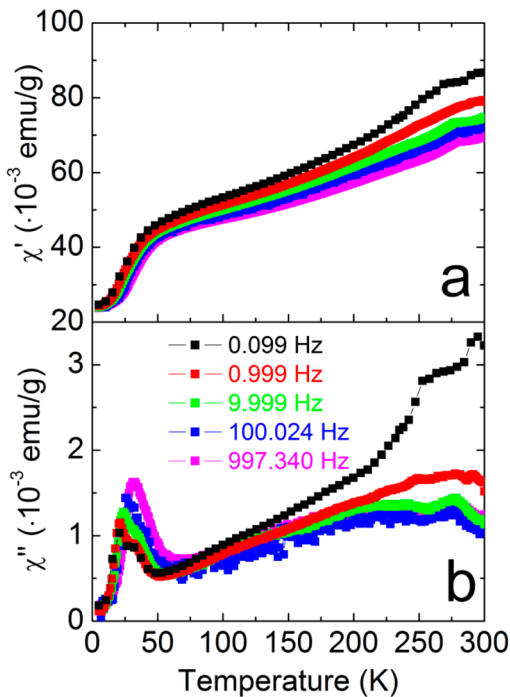


Figure 5. Frequency dependent real part, $\chi'(T)$, (a) and imaginary part, $\chi''(T)$, (b) of the ac susceptibility, for the NP2-1 sample.

cores may play an important role in their magnetic behavior. According to the latter, the phenomenological Vogel–Fulcher law has been utilized to fit the frequency dependence of the $\chi''(T)$ maximum at $T_{\max,l}$ (eq S2 and Figure S7b, Supporting Information). The resultant values for τ_0 ($\sim 10^{-6}$ s) are comparable to those in the literature for particles with intermediate-strength dipolar interactions.^{39,40}

At the same time, a power-law analysis (Supporting Information eq S3 and Figure S7c) could give the relaxation time in spin-glass systems, where strong dipolar interactions (superspin-glass response)^{41,42} or disordered surface spins³³ are observed. This latter approach results in reasonable values for the τ_0 ($\sim 10^{-4}$ s) and the critical exponential $zv = 6.9$. It is worth noting that such long τ_0 's have been observed before for the surface spin-glass freezing processes in Ni-ferrite^{33,43} and γ -Fe₂O₃ nanoparticles.⁴⁴

In order to distinguish which one among the Vogel–Fulcher or power laws (as both produce reasonable fit values) provide a more suitable phenomenological description of the spin dynamics, one can calculate the relative variation of the $\chi''(T)$ peak-temperature position per frequency decade, ψ ($= \Delta T/(T \Delta \log f)$), known as the Mydosh parameter. The calculated value of the ψ for the sample NP2-1 is 0.126. It falls in the range that predicts a blocking temperature with intermediate strength dipolar interactions among the magnetic moments ($0.05 < \psi < 0.13$) and not due to a spin-glass state, the range of which is $0.005 < \psi < 0.05$.⁴⁵

On the other hand, in order to distinguish experimentally the likelihood of a possible spin-glass state at $T_{\max,l}$, the impact of a dc

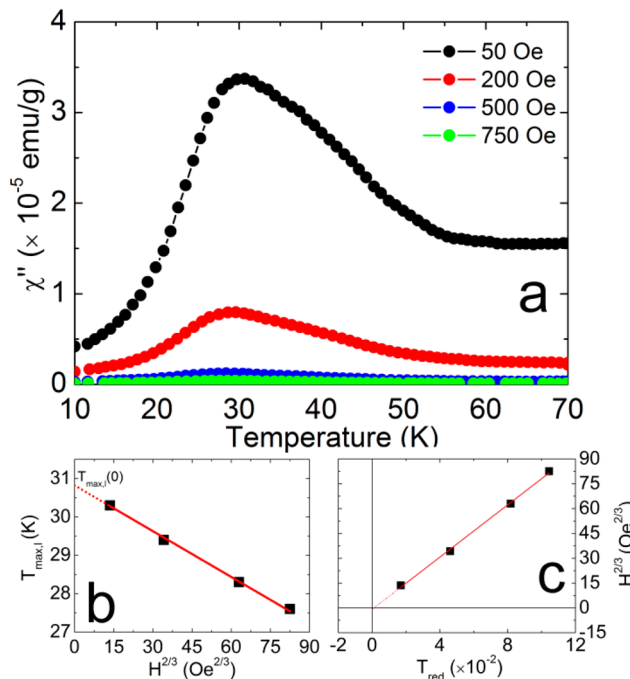


Figure 6. Temperature dependence of the imaginary part, $\chi''(T)$, of the ac susceptibility under dc magnetic fields from 50 to 750 Oe (a) and the field dependence of the freezing temperature, $T_{\max,l}$, for the NP2-1 sample. (b) The line is a fit with the Almeida–Thouless law ($\Delta T_{\max} \sim H^{2/3}$) and the $T_{\max,l}(0)$ extrapolated temperature for $H = 0$ Oe. $H^{2/3}$ versus reduced temperature, T_{red} ($T_{\text{red}} = 1 - T_{\max,l}(H)/T_{\max,l}(0)$) curve (c).

magnetic field, H , on the system dynamical behavior was investigated (Figure 6a). The temperature $T_{\max,l}$ was found to decrease with raising the magnetic field strength according to the Almeida–Thouless law (Figure 6b).⁴⁶ This behavior has been observed either in superparamagnetic or weakly interacting ferrimagnetic particles,³⁹ as well as for the spin-glass state of surface disordered spins.^{40,47} To resolve this, we utilized a criterion which rests on the relative offset of the $H^{2/3}$ vs T_{red} extrapolated line with respect to the origin. $T_{\text{red}} = 1 - T_{\max,l}(H)/T_{\max,l}(0)$ is the reduced temperature and $T_{\max,l}(0) = 30.8$ K is the extrapolated temperature for $H = 0$ Oe. In the general case, the existence of such an offset corroborates to superparamagnetic behavior (Figure 6c).^{48,49}

Overall, the above experimental evidence for NP2-1 together with the literature data are in favor of describing the frequency dependence of the $\chi''(T)$ maximum at $T_{\max,l}$ on the basis of the Vogel–Fulcher law. The absence of the individual single core NPs in the NP2-1 sample suggests that the sharp maximum of the imaginary part of the susceptibility at ~ 40 K can originate from mesocrystals involving a larger distance between single cores at the center of the NP assembly, as is discussed in the previous section (Figure 2a) on the effect of the dodecyl periphery. Due to their relative longer interparticle separation this may point to weaker dipolar interactions than those giving rise to the high-temperature broader maximum and the

Table 2. Analysis of the Relaxation Times, for the Sample NP2-1, on the Basis of the Arrhenius, Vogel–Fulcher, and Power-Law Phenomenological Descriptions (equations S1–S3, Supporting Information) of the Spin Dynamics

Arrhenius law		Vogel–Fulcher law			power law		
τ_0 (s)	E_a/k_B (K)	τ_0 (s)	E_a/k_B (K)	T_0 (K)	τ_0 (s)	zv	T^* (K)
3.3×10^{-10}	419.8 ± 27.0	2.1×10^{-6}	99.3 ± 9.1	11.8 ± 1.4	9.2×10^{-4}	6.9 ± 0.4	14.2 ± 3.3

Table 3. Results of DMEC Hydrogenation Using Pd-Containing Magnetically Separable Catalysts

catalyst notation	Pd content (wt %) ^a	Pd NP size (nm)	Pd NP size distribution (%)	TOF ₅₀ (s ⁻¹)	selectivity (%)	
					at 50% of the DMEC conversion	at 95% of the DMEC conversion
NP1-1-PdNP	3.2	-	-	0.7	94.7	92.8
NP1-2-PdNP	2.9	-	-	0.6	97.5	95.7
NP2-1-PdNP	4.3	1.2	11	14.7	98.4	97.1
2nd use	"	"	"	14.5	98.1	96.9
10th use	"	"	"	14.6	98.0	96.7
NP3-1-PdNP	3.5	2.7	30	5.0	98.0	97.3
Lindlar catalyst (Pd/CaCO ₃ poisoned by lead)	5	-	-	2.1	96.1	95.3

^aThe Pd content was determined by XRF analysis.

associated ferrimagnetic behavior. For the NP1-1 mesocrystals, this larger distance between single cores is not realized (Supporting Information Figure S3), thus resulting in the absence of additional superparamagnetic-like features in the low-*T* regime. The aforementioned discussion suggests that *the observed magnetic properties depend on the type of the dendron that has been employed for the mesocrystal stabilization* in each case.

Influence of Dodecyl Periphery on Pd Nanoparticle Formation

Formation. In this work iron oxide NPs were designed as a support for magnetically recoverable catalysts. Because iron oxide NPs are coated with polyphenylenepyridyl dendrons, catalytic Pd species coordinate with pyridyl groups and then Pd NP formation occurs upon reduction as was established in our preceding papers.^{11,12} Although we demonstrated different Pd NP sizes for different dendrons and dendrimers,¹² a sophisticated design of the catalysts was not carried out. Pd NP sizes were rather unpredictable because they depended on numerous factors such as the Pd species loading, the rate of reduction, and the Pd species exchange between dendrons in the iron oxide NP shell. The last factor is most uncontrollable as it depends on many aspects of the dendron structure. Thus, a logical step was designing a protective exterior, i.e., dodecyl chains on the dendron periphery.

It is worth noting that interaction of dendron-stabilized iron oxide NPs with Pd acetate was demonstrated to lead to the formation of aggregates which allow fast magnetic separation.^{11,12} In the case of dendrons with dodecyl periphery as capping molecules, aggregates also form, but their sizes do not exceed 1–2 μm (Figure S8, Supporting Information). This allows us to consider these catalysts for further use in microreactors where the aggregate size needs to be limited to a few micrometers and well controlled.

Reduction of Pd-containing magnetic nanocomposite with hydrogen normally leads to Pd NP formation.^{11,12} To our surprise, in the TEM image of the NP1-1PdNP nanocomposite no Pd NPs were observed after reduction (Figure S9, Supporting Information). At the same time, Pd was detected in this nanomaterial by elemental analysis (Table 3). Similar results were obtained for NP1-2-PdNP (images are not shown). On the other hand, for the nanocomposite stabilized by dendron 3 (second generation dendron with partial dodecyl periphery), the reduction resulted in comparatively large (2.7 nm) Pd NPs with broad NP size distribution, while in the case of dendron 2, nearly monodisperse 1.2 nm NPs (11% standard deviation) have been formed. HRTEM image of the NP2-1-PdNP sample presented in Figure 7 shows these Pd NPs (red arrows) around and on the top of iron oxide NPs (yellow arrows).

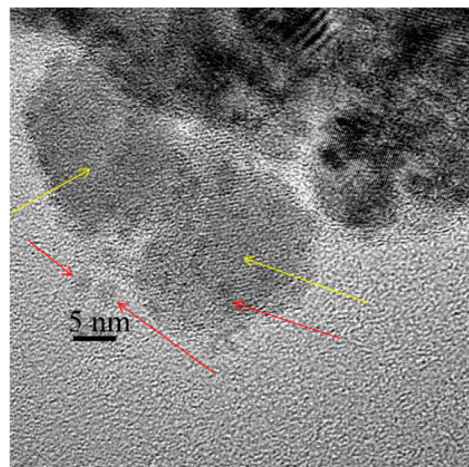


Figure 7. HRTEM image of NP2-1-PdNP. Pd NPs are indicated by red arrows. Larger iron oxide NPs are shown by yellow arrows.

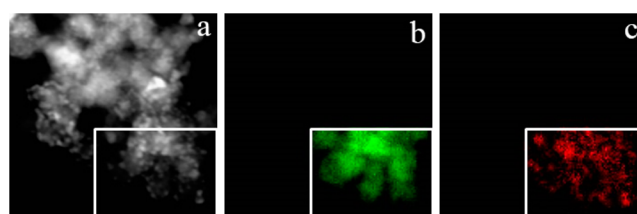


Figure 8. Dark-field STEM image (a) and Fe (b) and Pd (c) EDS maps of the NP2-1-PdNP sample.

To prove that indeed such morphology exists, we carried out EDS. A dark-field STEM image and EDS mapping of the NP2-1-PdNP sample presented in Figure 8 clearly show superposition of Pd on Fe indicating that Pd NPs are grown in the iron oxide NP dendron shells.

We propose the following explanation of differences in the Pd NP formation depending on the dendron structure. We assume that, for dendron 1, exchange of Pd species between dendrons is nearly prohibited. Each dendron contains six pyridines and can coordinate not more than six Pd atoms. When reduction is carried out with hydrogen, it penetrates well the nanocomposite aggregates allowing uniform and fast nucleation with the formation of a large amount of nuclei.⁵⁰ In the absence of the exchange between dendrons carrying Pd species, the Pd NP sizes are significantly below 1 nm (subnanometer particles). These Pd NPs cannot be seen in the nanocomposite because of the dark background provided by iron oxide NPs and comparatively thin dendron shells.

When the dendron has only half of the dodecyl chains as shown in Scheme 1 for 3, the exchange of Pd species between dendrons is not prevented. Moreover, because this dendron is asymmetrical, its packing on the iron oxide NP surface is likely to be not dense. Both factors lead to 2.7 nm Pd NPs, although in both NP1-1-PdNP and NP3-1-PdNP, the Pd content is nearly the same (Table 3). The third generation dendron with fully dodecyl periphery, 2, contains 14 nitrogen atoms which are readily available to complex with Pd acetate and to stabilize Pd NPs. Considering that each 1.2 nm Pd particle contains approximately 50 Pd atoms, the exchange between dendrons does take place, but it is minimal and well-controlled (narrow NP size distribution) revealing that dodecyl chains significantly diminish this process.

Thus, both generation and periphery of the dendrons allows us to control the Pd NP size.

Influence of the Pd NP Sizes on Catalytic Behavior. To assess the influence of the nanomaterial morphology on catalytic performance, NP1-1-PdNP, NP1-2-PdNP, NP2-1-PdNP, and NP3-1-PdNP were tested in selective hydrogenation of DMEC to DMVC (Scheme 2). DMVC is an intermediate for fragrant substances and vitamins E and K.⁵¹

Scheme 2. DMEC Hydrogenation with DMVC Being a Target Product and 2-Methylbutane-2-ol Being a Side Product

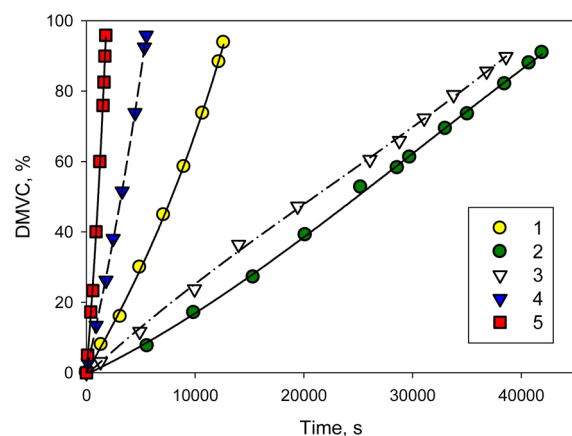
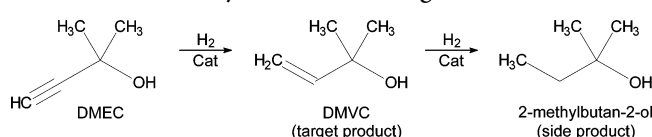


Figure 9. Kinetic curves of DMVC accumulation with Lindlar catalyst (1), NP1-2-PdNP (2), NP1-1-PdNP (3), NP3-1-PdNP (4), and NP2-1-PdNP (5).

The data of catalytic testing are presented in Table 3 and Figure 9. The TOF values in hydrogenation with NP1-1-PdNP and NP1-2-PdNP (i.e., two catalysts based on dendron 1 when Pd NP sizes are below resolution for these nanomaterials) are exceptionally low. The conversion after \sim 8 h did not exceed 65%. In the case of NP3-1-PdNP with 2.7 nm Pd NPs, the TOF is higher and conversion reaches 98% but selectivity does not exceed 95.1% at 95% of the DMEC conversion. For NP2-1-PdNP containing 1.2 nm Pd NPs, the reaction is very fast and the selectivity is 96.9% at 99% conversion.

Considering that the Pd NP environment is similar in all three dendrons, we believe the major factor influencing the catalytic properties is the Pd NP size. The traditional thinking is

smaller catalytic NPs allow higher catalytic activity due to higher NP surface area. Nevertheless, there is a number of studies demonstrating that an optimum catalytic NP size is required for the best catalytic activity.^{19–23} Apparently, Pd NPs significantly below 1 nm formed in NP1-1-PdNP and NP1-2-PdNP are below the threshold for efficient catalytic NPs,²⁰ while the 1.2 nm Pd NPs represent an optimum size, the influence of which can be attributed to the maximum amount of the effective catalytic sites on the NP surface.¹⁹

A magnetic separation was applied to NP2-1-PdNP for testing in 10 consecutive catalytic reactions. No catalyst loss was observed at every separation as the catalyst was not removed from the reaction vessel. It was situated at the side of the reactor using a rare earth magnet and washed in the same way directly in the reactor. This would be impossible if using filtration (typically employed for heterogeneous catalysts⁵²). The data of Table 3 show that TOF and selectivity remain unaffected, revealing exceptional stability of this catalyst. It is worth noting that the NP2-1-PdNP catalyst is significantly more active and selective than the Lindlar catalyst (Table 3) which is conventionally used in selective hydrogenation¹¹ or any other magnetically recoverable catalyst studied by us earlier.¹²

CONCLUSION

We demonstrated control over iron oxide and Pd NP formation using polyphenylenepyridyl dendrons of the second and third generations with dodecyl periphery. For iron oxide NPs, the dendron generation allows significant variation of the NP size, while stabilizing well comparatively large NPs. The Pd NP formation is finely regulated by both the generation and the amount of dodecyl chains on the dendron periphery. At the same time, it has also been shown that the dendron generation influences the internal structure of iron oxide multicore mesocrystals and, as such, it provides a sensitive nanoscale control of the associated magnetic properties. Furthermore, the catalytic activity was found to depend on the size of the Pd NPs that were immobilized on the mesocrystals.

Thus, we proposed a strategy for the smart design of novel catalysts. Exceptional catalytic properties of these nanomaterials, as well as the easy catalyst recovery, successful repeated cycle use, and the catalyst stability make them promising for hydrogenation and great potential for a number of other catalytic reactions carried out with Pd catalysts.

ASSOCIATED CONTENT

Supporting Information

Synthetic procedures, TEM images, XRD, TGA, SAXS data, and magnetic characteristics. This material is available free of charge via the Internet at <http://pubs.acs.org>.

AUTHOR INFORMATION

Corresponding Authors

*E-mail: shifrina@ineos.ac.ru (Z.B.S.).

*E-mail: lybronst@indiana.edu (L.M.B.).

Author Contributions

The manuscript was written through contributions of all authors.

Notes

The authors declare no competing financial interest.

ACKNOWLEDGMENTS

The financial support of this work was provided in part by funding from the European Community's Seventh Framework

Programme [FP7/2007-2013] under Grant Agreement No. CP-IP 246095, the NSF Grant CHE-1048613, the Ministry of Education and Science of Russia, and the Russian Foundation for Basic research under Grant Numbers 14-03-00876 and 14-03-31669.

■ REFERENCES

- (1) Hagen, J. *Industrial catalysis: A Practical Approach*; Wiley-VCH: Weinheim, Germany, 1999.
- (2) Astruc, D.; Boisselier, E.; Ornelas, C. *Chem. Rev.* **2010**, *110*, 1857–1959.
- (3) Wang, Z.; Shen, B.; Zou, A.; He, N. *Chem. Eng. J.* **2005**, *113*, 27–34.
- (4) Zhu, Y.; Peng, S. C.; Emi, A.; Su, Z.; Monalisa; Kemp, R. A. *Adv. Synth. Catal.* **2007**, *349*, 1917–1922.
- (5) Polshettiwar, V.; Luque, R.; Fihri, A.; Zhu, H.; Bouhrara, M.; Basset, J.-M. *Chem. Rev.* **2011**, *111*, 3036–3075.
- (6) Rossi, L. M.; Silva, F. P.; Vono, L. L. R.; Kiyohara, P. K.; Duarte, E. L.; Itri, R.; Landers, R.; Machado, G. *Green Chem.* **2007**, *9*, 379–385.
- (7) Saha, A.; Leazer, J.; Varma, R. S. *Green Chem.* **2012**, *14*, 67–71.
- (8) Vaddula, B. R.; Saha, A.; Leazer, J.; Varma, R. S. *Green Chem.* **2012**, *14*, 2133–2136.
- (9) Sun, W.; Li, Q.; Gao, S.; Shang, J. K. *Appl. Catal. B: Environ.* **2012**, *125*, 1–9.
- (10) Wang, D.; Astruc, D. *Chem. Rev.* **2014**, *114*, 6949–6985.
- (11) Kuchkina, N. V.; Yuzik-Klimova, E. Y.; Sorokina, S. A.; Peregovodov, A. S.; Antonov, D.; Nikoshvili, L. Z.; Sulman, E. M.; Morgan, D. G.; Gage, S. H.; Mahmoud, W. E.; Al-Ghamdi, A. A.; Bronstein, L. M.; Shifrina, Z. B. *Macromolecules* **2013**, *46*, 5890–5898.
- (12) Yuzik-Klimova, E. Y.; Kuchkina, N. V.; Sorokina, S. A.; Boris, B.; Morgan, D. G.; Nikoshvili, L. Z.; Lyubimova, N. A.; Matveeva, V. G.; Sulman, E. M.; Stein, B. D.; Svergun, D. I.; Spilotros, A.; Kostopoulou, A.; Lappas, A.; Shifrina, Z. B.; Bronstein, L. M. *RSC Adv.* **2014**, *4*, 23271–23280.
- (13) Newkome, G. R. *Advances in dendritic macromolecules*; JAI Press: Greenwich, 1994; Vol. 1.
- (14) Balzani, V.; Campagna, S.; Denti, G.; Juris, A.; Serroni, S.; Venturi, M. *Acc. Chem. Res.* **1998**, *31*, 26–34.
- (15) Bronstein, L. M.; Shifrina, Z. B. *Chem. Rev.* **2011**, *111*, 5301–5344.
- (16) Yeung, L. K.; Crooks, R. M. *Nano Lett.* **2001**, *1*, 14–17.
- (17) Knecht, M. R.; Garcia-Martinez, J. C.; Crooks, R. M. *Chem. Mater.* **2006**, *18*, 5039–5044.
- (18) Gates, A. T.; Nettleton, E. G.; Myers, V. S.; Crooks, R. M. *Langmuir* **2010**, *26*, 12994–12999.
- (19) Wei, G.-F.; Liu, Z.-P. *Phys. Chem. Chem. Phys.* **2013**, *15*, 18555–18561.
- (20) Mukherjee, S.; Ramalingam, B.; Griggs, L.; Hamm, S.; Baker, G. A.; Fraundorf, P.; Sengupta, S.; Gangopadhyay, S. *Nanotechnology* **2012**, *23*, 485405–485418.
- (21) Viswanathan, V.; Wang, F. Y.-F. *Nanoscale* **2012**, *4*, 5110–5117.
- (22) Yu, T.; Wang, W.; Chen, J.; Zeng, Y.; Li, Y.; Yang, G.; Li, Y. *J. Phys. Chem. C* **2012**, *116*, 10516–10521.
- (23) Valden, M.; Lai, X.; Goodman, D. W. *Science* **1998**, *281*, 1647–1650.
- (24) Konarev, P. V.; Volkov, V. V.; Sokolova, A. V.; Koch, M. H. J.; Svergun, D. I. *J. Appl. Crystallogr.* **2003**, *36*, 1277–1282.
- (25) Svergun, D. I. *J. Appl. Crystallogr.* **1992**, *25*, 495–503.
- (26) Franke, D.; Svergun, D. I. *J. Appl. Crystallogr.* **2009**, *42*, 342–346.
- (27) Morgan, D. G.; Boris, B. S.; Kuchkina, N. V.; Yuzik-Klimova, E. Y.; Stein, B. D.; Svergun, D. I.; Spilotros, A.; Kostopoulou, A.; Lappas, A.; Shifrina, Z. B.; Bronstein, L. M. *Langmuir* **2014**, *30*, 8543–8550.
- (28) Niederberger, M.; Coelfen, H. *Phys. Chem. Chem. Phys.* **2006**, *8*, 3271–3287.
- (29) Von Hoene, J.; Charles, R. G.; Hickam, W. M. *J. Phys. Chem.* **1958**, *62*, 1098–1101.
- (30) Qi, X.; Xue, C.; Huang, X.; Huang, Y.; Zhou, X.; Li, H.; Liu, D.; Boey, F.; Yan, Q.; Huang, W.; De Feyter, S.; Mullen, K.; Zhang, H. *Adv. Funct. Mater.* **2010**, *20*, 43–49.
- (31) Svergun, D. I. *Biophys. J.* **1999**, *76*, 2879–2886.
- (32) Kostopoulou, A.; Brintakis, K.; Vasilakaki, M.; Trohidou, K. N.; Douvalis, A. P.; Lascialfari, A.; Manna, L.; Lappas, A. *Nanoscale* **2014**, *6*, 3764–3776.
- (33) Nadeem, K.; Krenn, H.; Traussing, T.; Letofsky-Papst, I. *J. Appl. Phys.* **2011**, *109*, 013912/1–013912/6.
- (34) Winkler, E.; Zysler, R. D.; Mansilla, M. V.; Fiorani, D.; Rinaldi, D.; Vasilakaki, M.; Trohidou, K. N. *Nanotechnology* **2008**, *19*, 185702/1–185702/8.
- (35) Sharma, S.; Ningthoujam, R. S.; Gajbhiye, N. S. *Chem. Phys. Lett.* **2013**, *558*, 48–52.
- (36) Neel, L. C. R. *Hebd. Seances Acad. Sci.* **1949**, *228*, 664–666.
- (37) Saslow, W. M. *Phys. Rev. B* **1988**, *37*, 676–678.
- (38) Levy, L. P.; Ogielski, A. T. *Phys. Rev. Lett.* **1986**, *57*, 3288–3291.
- (39) Peddis, D.; Rinaldi, D.; Ennas, G.; Scano, A.; Agostinelli, E.; Fiorani, D. *Phys. Chem. Chem. Phys.* **2012**, *14*, 3162–3169.
- (40) Tackett, R. J.; Bhuiya, A. W.; Botez, C. E. *Nanotechnology* **2009**, *20*, 445705/1–445705/7.
- (41) Suzuki, M.; Fullem, S. I.; Suzuki, I. S.; Wang, L. Y.; Zhong, C. J. *Phys. Rev. B* **2009**, *79*, 024418/1–024418/7.
- (42) Parker, D.; Dupuis, V.; Ladieu, F.; Bouchaud, J. P.; Dubois, E.; Perzynski, R.; Vincent, E. *Phys. Rev. B* **2008**, *77*.
- (43) Jaffari, G. H.; Rumaiz, A. K.; Woicik, J. C.; Shah, S. I. *J. Appl. Phys.* **2012**, *111*, 093906/1–093906/6.
- (44) Nadeem, K.; Krenn, H.; Traussig, T.; Wurschum, R.; Szabo, D. V.; Letofsky-Papst, I. *J. Appl. Phys.* **2012**, *111*, 113911/1–113911/6.
- (45) Nadeem, K.; Krenn, H.; Traussig, T.; Wurschum, R.; Szabo, D. V.; Letofsky-Papst, I. *J. Magn. Magn. Mater.* **2011**, *323*, 1998–2004.
- (46) Dealmeida, J. R. L.; Thouless, D. J. *J. Phys. A: Math. Gen.* **1978**, *11*, 983–990.
- (47) Gajbhiye, N. S.; Bhattacharyya, S. *Mater. Chem. Phys.* **2008**, *108*, 201–207.
- (48) Peddis, D.; Cannas, C.; Musinu, A.; Piccaluga, G. *J. Phys. Chem. C* **2008**, *112*, 5141–5147.
- (49) Dormann, J. L.; Fiorani, D.; Elyamani, M. *Phys. Lett. A* **1987**, *120*, 95–99.
- (50) Shtykova, E. V.; Svergun, D. I.; Chernyshov, D. M.; Khotina, I. A.; Valetsky, P. M.; Spontak, R. J.; Bronstein, L. M. *J. Phys. Chem. B* **2004**, *108*, 6175–6185.
- (51) Bonrath, W.; Eggersdorfer, M. *Catal. Today* **2007**, *121*, 45–57.
- (52) Das, P.; Aggarwal, N.; Guha, N. R. *Tetrahedron Lett.* **2013**, *54*, 2924–2928.